Component analysis of a 25-cell stack following 6.7 kh of high temperature electrolysis

Jérôme Aicart, Karine Couturier, Maxime Hubert, Karl Vulliez, Manon Elie, Lucas Champelovier, Nathalie Giacometti, Marie Petitjean, Bertrand Morel, Brigitte Gonzalez, et al.

To cite this version:

Jérôme Aicart, Karine Couturier, Maxime Hubert, Karl Vulliez, Manon Elie, et al.. Component analysis of a 25-cell stack following 6.7 kh of high temperature electrolysis. International Journal of Hydrogen Energy, 2024, 93, pp.562-573. 10.1016/j.ijhydene.2024.11.045 . cea-04844470

Component Analysis of a 25-Cell Stack Following 6.7 kh of High Temperature Electrolysis

J. Aicart [1*], K. Couturier [1], M. Hubert [1], K. Vulliez [1], M. Elie [1], L. Champelovier [1], N. Giacometti [1], M. Petitjean [1], B. Morel [1], B. Gonzalez [1], M. Prioux [1], K. Henault [1], S. Di Iorio [1], A. Laplace [2], J.G. Begos [2], C. Vallat [2], E. Régnier [2], R. Moles [2], T. David [1], T. L. Lai [1], J. Laurencin [1]

(1) Univ. Grenoble Alpes, CEA-Liten, 38000 Grenoble, France
(2) Univ. Montpellier, CEA-ISEC, 30207 Bagnols-sur-Cèze, France

[*] Corresponding author: jerome.aicart@cea.fr

Abstract (150/150 words)

The demonstration of relevant lifetimes for solid oxide electrolysis stacks is an underlying necessity to the rapidly industrializing technology. Following a 6.7 kh test of a 25-cell stack, post-mortem analyses of cells, seals, and interconnects were carried out to assess their long-term stability.

Micrographs of cells aged in nominal conditions highlighted Ni depletion in the functional layer, SZO interlayer growth, and the presence of a Sr-rich secondary phase. The microstructure of glass-ceramic seals remained for the most part stable following operation. In addition, in spite of a thin design and the absence of coating, interconnects showed remarkable stability, with limited chromia growth and Cr depletion. Notably, no Cr poisoning could be detected in the cell functional layer.

In view of the results, the loss of tightness of the H_2 compartment, due to initial defects or caused by failures, is seen as the most immediate threat to this stack long-term operation.

Highlights (4, max 75 characters including spaces)

- Post-mortem analyses of a SOEC stack following 6.7 kh of operation
- Aged thin interconnects and glass seals showed little evolutions
- Ni migration and SZO formation evidenced on aged cells
- Final OCV data suggests onset of tightness failure of 1 of the 25 cells

Keywords

Electrolysis ; Durability ; Interconnect ; Post-mortem analysis ; Sealing, Solid Oxide Electrolysis ; Stack

1. Introduction

To become a competitive low-carbon economy by 2050, the European Commission has to rethink clean energy supply policies [1]. Hydrogen is expected to play a key role in this transition, with a share in the European Union energy mix skyrocketing from 2% currently to 14% in 2050 [2]. Thus, a deployment plan targeting 100 GW of electrolysis power has been proposed [3]. While alkaline and proton exchange membrane water electrolyzes should remain dominant in the upcoming years due to their higher maturity, solid oxide electrolysis (SOE) is able to achieve the highest DC power-to-H_2 efficiencies. The highly promising technology [4,5] could bring the levelized cost of hydrogen (LCOH) down to 2 € kg^{-1} for electrolysis plants at the scale of hundreds of MW with an electricity cost of 40 € MWh^{-1} [6]. At the core of the technology, solid oxide cells (SOC) are typically operated over a fraction of the 550-to-850°C temperature range, depending on architecture, and stacked to increase the overall power density.

The technology has recently entered a phase of aggressive industrialization, and several MW-scale demonstration units are being commissioned (Bloom Energy 4 MW, Sunfire 2.4 MW, Ceres 1 MW). However, significant efforts are still required to turn the high efficiencies into a competitive LCOH. As long as such cost remains largely controlled by that of stack manufacturing [7], degradation studies assessing the achievable lifetimes of stacks over relevant durations will remain a crucial subject of research and development.

The great majority of high temperature electrolysis (HTE) degradation studies found in the literature has been carried out at a set operating temperature. Consequently, degradation rates are generally expressed in terms of voltage increase or Area Specific Resistance (ASR) increase over time. However, in recent years, an increasing number of long-term stack testing has been carried out by gradually increasing the temperature in order to compensate degradation and maintain voltage levels around the thermoneutral equilibrium (i.e. about 1.29 V per SOC). This operation mode is noteworthy not only for achieving high energy-conversion efficiency but also for sustaining that efficiency over time. Furthermore, it limits thermal gradients within the stack/cells, whose impact on lifespan is not yet well understood. Degradation is then expressed in terms of temperature increase over time [8–12]. A third operating strategy consists in setting both temperature and voltage, yielding a decreasing current and H_2 production over time [13]. In this case, degradation rates are expressed in terms of current decrease over time.

Regarding long-term degradation studies carried out at cell level, Schefold et al. [14] operated an 6Sc1CeSZ (6 mol% Scandia 1 mol% ceria-stabilized zirconia) electrolyte-supported cell

(ESC) composed of Ni-GDC (gadolinium-doped ceria) and LSCF (lanthanum strontium cobalt ferrite) as H_2 and O_2 electrodes, respectively, in SOEC mode at various current densities for 23 kh. The +7.4 mV kh^{-1} (or +0.57 %U kh^{-1}) voltage degradation was attributed to electrolyte conductivity decay, interlayer formation and O_2 electrode delamination. Later on, the same authors recorded an impressive 34 kh electrolysis test [15] on a similar cell (with 10Sc1CeSZ electrolyte), at -0.6 A cm^{-2} and 50% steam conversion (SC). Electrochemical impedance spectroscopy (EIS) data pointed to a mostly ohmic cell degradation. A similar conclusion was reached by Schefold et al. [16] following an uninterrupted 30 kh electrolysis test of a 45 cm^2 3YSZ (3 mol% yttria-stabilized zirconia) ESC operated at 60% SC, -0.7 and -0.9 A cm^{-2}, over the 851 to 858°C temperature range.

Regarding degradation studies at short stack level, Fang et al. [17] operated a cathode-supported 2-cell stack (CSS, the cathode being the hydrogen electrode in electrolysis mode) for more than 20 kh, most of which spent in electrolysis mode at 800°C, -0.5 A cm^{-2} and 50% SC. The in-house cells were made of standard materials Ni-YSZ/8YSZ/LSCF. They reported a ~+0.6%U kh^{-1} voltage degradation rate. Post mortem analyses evidenced air electrode and barrier layer delamination, Ni depletion, and demixing of the air electrode, while noting that the external gas tightness of the stack after testing was similar to new stacks [18]. Another (6-cell) short stack was operated for 10.7 kh in electrolysis mode by Rinaldi et al. [19]. The authors reported a +0.5 %U kh^{-1} degradation at 720°C, -0.5 to -0.6 A cm^{-2} and a SC from 42% to 50%. Post mortem analyses highlighted Ni depletion, void formation in the 8YSZ electrolyte, $SrZrO_3$ formation, and Si and Cr accumulation [19]. Recently, Riegraf et al. [20] operated a 10-cell stack over approximately 3.3 kh at -0.6 A cm^{-2}, 75% SC, and 816°C. These conditions yielded a negative overall degradation rate of -0.33 %U kh^{-1}, while EIS data recorded at stack level highlighted an increase of the ohmic resistance balanced by a decrease of the polarization resistance [20].

The scale up from single cells to stacks introduces additional degradation mechanisms (e.g. interconnect oxidation [21]). While separating the cell contribution to the overall degradation from that of the stack remains challenging, Léon et al. [10] could determine that the degradation rate of a 30-cell stack (+10.5 mV kh^{-1}) was about twice that of the constituting electrolyte-supported cells (ESC, Ni-GDC/3YSZ/GDC/LSCF, +5 mV kh^{-1}), when operated at 830°C and -0.5 A cm^{-2}. Lang et al. [8] tested a 30-cell electrolyte-supported stack over 7.5 kh, 3.4 kh of which were spent in SOEC mode, 820°C, -0.52 A cm^{-2} and 70% SC. They recorded a combined evolution of +0.5%U kh^{-1} for the voltage and +3.0 K kh^{-1} for the stack temperature, and determined the degradation was mostly ohmic. Walter et al. [9] operated a similar stack for 9 kh, 8 kh of which spent in SOEC mode alternating between -0.25, -0.5 and -0.65 A cm^{-2}. While this study did not report post-mortem analysis results, the authors attributed the added degradation compared to SOFC stacks mainly to Si contamination in the Ni-GDC electrode. Additionally, several very long-term durability tests have been conducted at full stack level and beyond to provide overall degradation rates without attributing the results to identified mechanisms [11,12,22–24].

Following a previous 6.7 kh stack test [11], which remains to date the longest operating time achieved with our proprietary stack design, several post-mortem analyses were carried out with the intent of evaluating the long-term stability of the stack base components. Samples of cells, interconnects, and glass-ceramic seals were therefore observed by scanning electron microscopy, and the results have been compiled in the present paper. While the test data at stack level was shared in the initial publication [11], this work also highlights the heterogeneities recorded among the 25 individual cell voltages, the homogeneity of the recorded temperature field, and provides additional insights on the evolution of stack tightness over time.

2. Experimental

2.1. Stack Test

The stack was manufactured in-house, and incorporated a self-clamping solution for mechanical compression [25,26]. Based on a proprietary design, this stack comprised thin interconnects out of AISI441 ferritic stainless steel, and 25 commercial cathode-supported cells with a 100 cm^2 active area. The iron-based steel notably contained 17.5 wt% of chromium, 0.5 wt% of titanium and niobium, 0.4 wt% of silicon and 0.25 wt% of manganese. The cells, all from the same design, exhibited a Ni-8YSZ cermet fuel electrode, an 8YSZ electrolyte, a GDC diffusion barrier, and a LSC (lanthanum strontium cobaltite) oxygen electrode. LSM (strontium-doped lanthanum manganite) coatings and nickel meshes ensured sufficient electrical contact between electrodes and interconnects on the oxygen and hydrogen sides, respectively. Tightness of both anodic and cathodic compartments was achieved through a combination of mica foils and glass-ceramic seals. The seals came from the $MgO-Al_2O_3-BaO-SiO_2-B_2O_3$ glassy system that has shown a good compliance with the seal specifications [27–29]. In order to deposit and shape the seal, a suspension composed of the glass powder (d_{50}= 16 ± 4 μm), organic solvents and adjuvants, was used. After the deposition of the suspension on the areas to be sealed (stainless steel interconnects, mica foils), a heat treatment allowed obtaining a glass-ceramic.

The test was carried out on an in-house bench [25,30], with preheating loops installed around the stack to insure that inlet gas temperature was that of the furnace. The bench incorporated 8 programmable logic controller (PLC) channels dedicated to the monitoring of repeating unit (RU) voltages. RUs consist in assembly of two half-interconnects, where the voltage probes are welded on, their respective contact elements, and a SOC. Given the 25 RUs of the stack, and the lack on in-house data at full stack level beyond 5 kh, this was considered a limitation. To increase the instrumentation level, an external data acquisition system was installed (KeySight 34980A) to record all individual RU voltages (KeySight 34921A). However, no communication could be implemented at the time between the external system and the PLC. Throughout the test, the stack direct environment was instrumented with five type-K thermocouples: 2 in the stack top plate (TP), 2 in the bottom plate (BP), and one measuring the air outlet (AO) temperature.

During operation, the stack was maintained in near-thermoneutral conditions through gradual and intentional increase of the furnace temperature to compensate degradation. Steam conversion (SC) was set to 70% whenever applicable. The overall test sequence started and ended with a current density of -0.65 A cm^{-2}. Corresponding stack temperature evolved from 670°C at the beginning of the test to 760°C at the end.

Additional details on stack design and performance, testing equipment, intended protocol and deviations can be found in the initial publications related to this work [11,31], and their subsequent references [32–38]. Overall, the stack was polarized for 6.7 kh. After disassembly, several post-mortem characterizations were carried out on cells, interconnects, and glass-ceramic sealing material.

2.2. Post-Mortem Characterization of Cells

A Field Emission Gun - Scanning Electron Microscope (FEG-SEM, ZEISS Merlin) has been used to observe the microstructure of selected cells of the stack. Before the characterization, pieces of cell were cut and embedded in an epoxy resin (Epofix®) under vacuum to fill the open porosity. Then, the cross-sections were polished step by step until a final stage using a diamond spray at 0.25 µm. To avoid charging effects during the observations, a thin carbon layer was deposited on the surface. The SEM images were done with a Back-Scattered Electrons (BSE) detector using an acceleration voltage of 2 kV. Moreover, some Energy Dispersive X-ray spectroscopy (EDX) maps have been recorded using an acceleration voltage of 10 kV. To assess microstructure evolutions, aged samples were compared to a pristine cell, observed directly following cermet reduction.

2.3. Post-Mortem Characterization of Interconnects

Big samples were cut with a motor saw from one stack interconnect in the 100 cm² active area facing the cell electrodes. They were cold embedded under pressure as cross-sections in an epoxy resin (Epofix®) to maintain the different layers in place and drive residual bubbles away from resin. Then they were cut in smaller samples that were progressively polished down to 1 µm and a finishing step with 0.04 µm alumina particles was carried out. A 5 nm carbon thin layer was deposited on each sample surface to improve electrical conduction and limit charging effects. SEM images were acquired at 10 kV acceleration voltage, with a BSE detector in a Zeiss Merlin SEM. EDX analyses were done with Bruker detectors at 10 kV.

To go further in the interconnect characterization, high lateral resolution image analyses were performed on cross-sections without carbon layer with a Time-of-Flight Secondary Ion Mass Spectrometry (ToF SIMS) instrument from IONTOF GmbH using Bi+ (30 keV) as primary ion species, in dual beam depth profiling mode to detect low Cr content to a depth of several microns.

2.4. Post-Mortem Characterization of Glass Ceramic Seals

Following the 6.7 kh of stack operation, seal samples were recovered between two interconnects at the fuel side, and prepared for SEM analysis. The recovered samples also contained mica foils. To assess seal material ageing from a crystallization point of view, the above-stated samples were compared with glass-ceramic samples obtained from the thermal treatment of the glassy powder. A 750°C target temperature was chosen from the stack temperature evolution. The glassy powder was heated at 5 °C min^{-1} in air to reach the target temperature for 48h, and was then air-cooled at the end of the treatment.

Polished sections of the different samples were analyzed using SEM (SUPRA 55 ZEISS, BRUKER Energy Dispersive Spectroscopy – EDS – detector) for microstructure and composition determination.

3. Results and Discussion

3.1. Durability Test Data

The test sequence included different galvanostatic steps at various current densities, a 530 h current cycling step, two thermal cycles, as well as initial/final performance characterizations. Table 1 breaks down the different steps and their corresponding durations. Overall, the stack spent 6.7 kh in operation. While the evolutions of stack current and voltage have been shared in [11,31], experimental results in terms of individual RU voltages, their average value, and temperatures are given in Figure 1a and b, respectively.

Initial maximum dispersion among the individually recorded 25 RU voltages was at a low 70 mV. However, throughout the 6.7 kh test sequence, increasing levels of voltage heterogeneity were evidenced. After only about 1.5 kh, the dispersion had increased to 134 mV, mostly due to the voltage of RU n°25 (U25) gradually dropping from an initial 1.25 V to 1.19 V. U25 remained significantly below the thermoneutral voltage for the remaining of the test, decreasing even further beyond 4 kh. Such a significant voltage drop may be explained by a feed distribution favoring RU25 over time. However, none of the two thermocouples located in close proximity of the cell, in the stack top end plate, recorded a temperature drop related to the apparent endothermic operation of RU25.

Early on, in addition to U25, six RU were showing peculiar behaviors. Most notably, the recorded Open Circuit Voltage (OCV) of RU_n (n=5,7,23) would be about 20 mV below the average and expected value, while that of RU_{n+1} would be 20 mV above. Faulty wiring material was thought to be the problem, and the three corresponding voltage probes were replaced when the stack was brought back to room temperature at 3.01 kh. No positive effect on the voltages was subsequently recorded once the stack had resumed operation. Eventually, through post-mortem SEM analyses, it was determined that the surprising voltage readings were indeed caused by probes made of different materials. A supplier error caused most of this stack probes to be made of pure Ni. The ones replaced at 3.01 kh were the only ones made of the expected Ni-Cr alloy and naturally, replacing them with Ni-Cr did not affect the measurements. Finally, the recorded deviations to the expected OCV was also experimentally verified to match the

Seebeck effect between Ni and NiCr materials, ranging from 20.3 mV at 715°C to 23.7 mV at 803°C. Consequently, while adding or subtracting that electromotive force associated to the Seebeck effect should give a pretty accurate estimation of individual voltages, only the 2-RU averages for RUs 5&6, 7&8, and 23&24, respectively, are given in Figure 1a for the sake of accuracy.

Table 1 : Description of the overall testing sequence with corresponding start times, end times, and durations. All galvanostatic steps were carried out at a steam conversion of 70%.

Step description	**Time start** / kh	**Time end** / kh	**Duration** / kh
Initial characterizations	0	0.27	0.27
Galvanostatic operation, -0.65 A cm^{-2}	0.27	1.44	1.17
Thermal cycle	1.44	1.6	N.A.
Galvanostatic operation, -0.65 A cm^{-2}	1.60	1.74	0.14
Galvanostatic operation, -0.85 A cm^{-2}	1.74	3.01	1.27
Thermal cycle	3.01	3.15	N.A
Galvanostatic operation, -0.85 A cm^{-2}	3.15	3.41	0.26
Cycling 4h OCV & 4h -0.50 A cm^{-2}	3.41	3.94	0.53
Galvanostatic operation, -0.50 A cm^{-2}	3.94	4.76	0.82
Galvanostatic operation, -0.65 A cm^{-2}	4.76	6.99	2.23
Final characterizations	6.99	7.02	0.03
		Total stack operation	6.72 kh

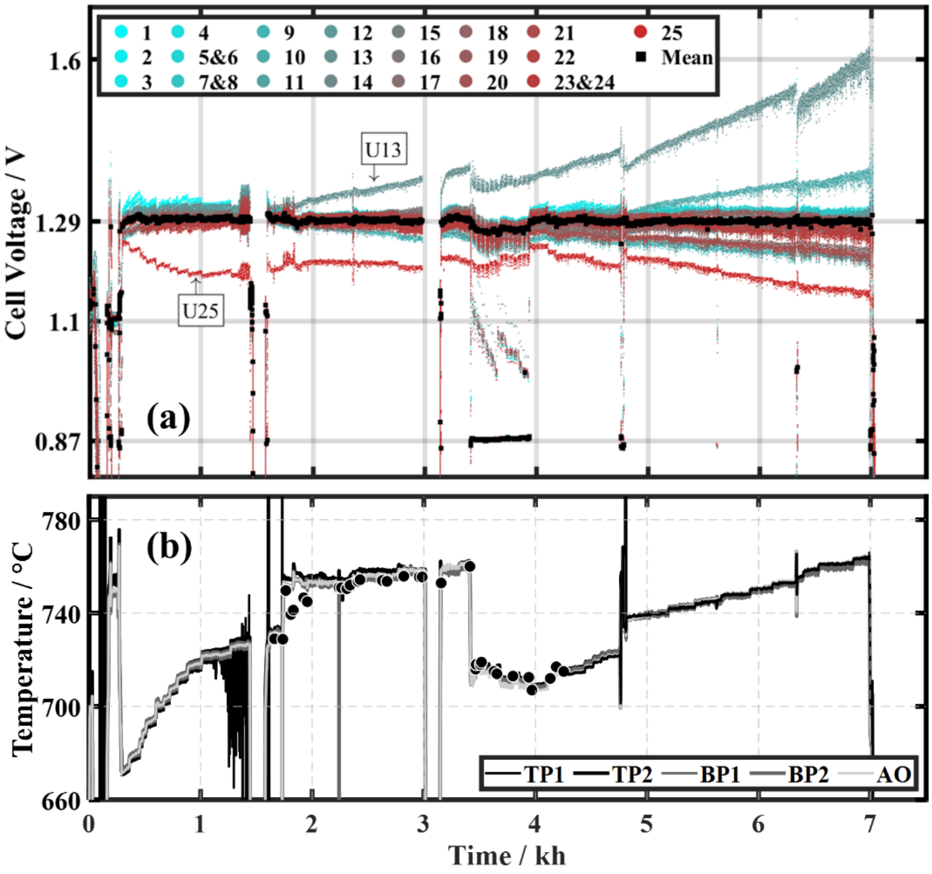

Figure 1 : a) Individual repeating unit voltages of the 25-cell stack with resulting average and b) stack temperature evolutions throughout the complete test sequence (TP: top plate, BP: bottom plate, AO: air outlet).

Stack temperature results are shown in Figure 1b. Overall, the data showed limited dispersion, underlining an effective thermoneutral operating strategy. After about 1 kh of testing, the measurement by sensor TP1 started to fluctuate significantly. The sensor was indeed losing its electrical insulation, and the corresponding PLC channel could not handle appropriately the stack voltage. Between 1.5 and 4.5 kh, the temperature was consequently checked periodically using a high insulation portable display. From 4.5 kh on, continuous data recording could resume after the sensor had been connected to the external data logger. Similarly, the thermocouple positioned in TP2, also polarized, failed abruptly after approximately 4.8 kh. Conversely, no issue was recorded with the other three temperature sensors that were either not or weakly polarized. This result emphases the relative fragility of the type-K thermocouples used in this work when polarized at high temperatures. Overall and due to the operating strategy, the stack temperature evolved from about 670°C to 760°C over the complete test sequence.

After approximately 1.33 kh of testing, in the middle of winter, the ventilation heating in the laboratory broke down. As a result, ambient temperature dropped below that of the cooling water, and condensation occurred and accumulated in the H_2 exhaust pipe. This led the stack pressure levels to fluctuate, impacting RU voltages to some extent (Figure 1a). As the pipe could not be drained with the stack still in operation, the bench was brought back to room temperature. Subsequent operation quickly highlighted an enhanced and accelerating degradation rate for RU13, suggesting local damage. Indeed, its voltage evolution rate increased from approximately +12 mV kh^{-1} between 0.3 and 1.3 kh to +47 mV kh^{-1} between 1.8 and 3 kh, and increased further to +96 mV kh^{-1} between 5 and 6.3 kh. Cell degradation was even more severe than these rates already suggest, as they were recorded in spite of an evolving operating temperature. Due to the extremely high voltage of damaged RU13 combined with the low value of U25, maximum voltage dispersion had increased to 202 mV after 5 kh, and up to 466 mV at the end of the test. Nevertheless, stable overall stack operation was then still evidenced.

3.2. Tightness Evolution over Time

The stack was first assembled on a production bench, where the seal and cermet conditioning procedures were then carried out. Prior to its subsequent integration to the test bench, the tightness of the air and fuel compartments was assessed at 20°C under air. Continuous air flowrates of 115 NmL min^{-1} and 69 NmL min^{-1} were necessary to sustain pressures of +30 mbarg on the air and fuel sides, respectively. Based on these results at room temperature, and reasonably assuming the leaks followed a viscous flow behavior, the leak-rates at 800°C could be estimated. Considering an inlet flowrate of 12 NmL min^{-1} cm^{-2} of 90/10 vol.% H_2O/H_2, corresponding with this stack architecture to a chamber pressure gradient of 100 mbar, the leak-rates for the air and fuel chambers were estimated at 0.15% and 0.09%, respectively (1.36% and 0.79% at room temperature). These results underline a sufficient initial tightness of the stack H_2 compartment, compatible with the duration objective of the testing protocol. Although the leak-rate of the air compartment was almost twice that of the fuel side, this had no consequence on stack operation in electrolysis mode.

Following the mounting in the test bench, and the initial temperature ramp from ambient, an Electrochemical Tightness Test (ETT) was carried out. It consisted in shutting off all inlet gases and measuring the rate of voltage decrease over time. The test was to end either after 20 min or when reaching a minimum voltage of 0.8 V, whichever came first [39], and can allow spatial identification of tightness defect. However, the ETT can also raise significantly the risk of Ni oxidation, particularly dangerous with cathode-supported cells, and must be carried out with caution. The test, shown in Figure 2a, only lasted less than 2 minutes, and all individual RU voltages where impacted. Consequently, a global tightness defect is assumed to have been located at one of the interfaces between the stack H_2 compartment and the bench. Given the relatively high OCVs in 6 NmL min^{-1} cm^{-2} of 95/5 vol% N_2/H_2 (Figure 2a), and the stack excellent initial performances at 70% SC [11,31], the defect is believed to have been located at the H_2 outlet. In addition, Figure 2a also shows additional local leaks on RU 13 and 19, but does not allow differentiating between a larger peripheral tightness defect, or a smaller crossover. The extent of the overall leak of the H_2 compartment was assessed through condensate collection experiments, carried out multiple times after approximately 5 kh of operation. Taking into account the cooling water temperature, and the resulting saturated vapor pressure, only 95.5% of theoretical condensates could then be collected, further confirming a macroscopic tightness defect.

Figure 2b shows the evolution of the deviation between theoretical and measured OCVs throughout the testing sequence, as measured in 90/10 vol% H_2O/H_2. Over the first 5 kh, the absolute deviation was below 0.5%, suggesting sufficient stack tightness and adequate bench control. However, beyond 5 kh, the OCV of cell 13, particularly impacted by the failure mode at 1.5 kh, and subsequently showing enhanced degradation rate and high voltage (Figure 1a), started to dip significantly. This trend could not be detected in real time by the test bench, which was only recording the combined voltage of RUs 13 to 16 [11,31], yet must be considered as the onset of cell failure. It is thus unlikely that the stack could have stayed operable for another few thousand hours, had the test continued. At this point, it is unclear if the peculiar initial ETT results for cell 13 can be correlated to its early signs of failure beyond 5 kh.

A final assessment of the stack overall tightness was carried out at room temperature after unmounting it from the bench, using the same method as previously described. Under the maximum flowrate of 100 NmL min^{-1} of N_2, the recorded pressure levels of the H_2 compartment were 4.5 mbar when the air side was open, and 4.9 mbar when closed. These results highlight a significant decrease of stack tightness throughout the complete test sequence, and underline a crossover. Evidently, achieving gas tightness at stack level remains challenging [40], especially as the number of repeating units and targeted test durations increase.

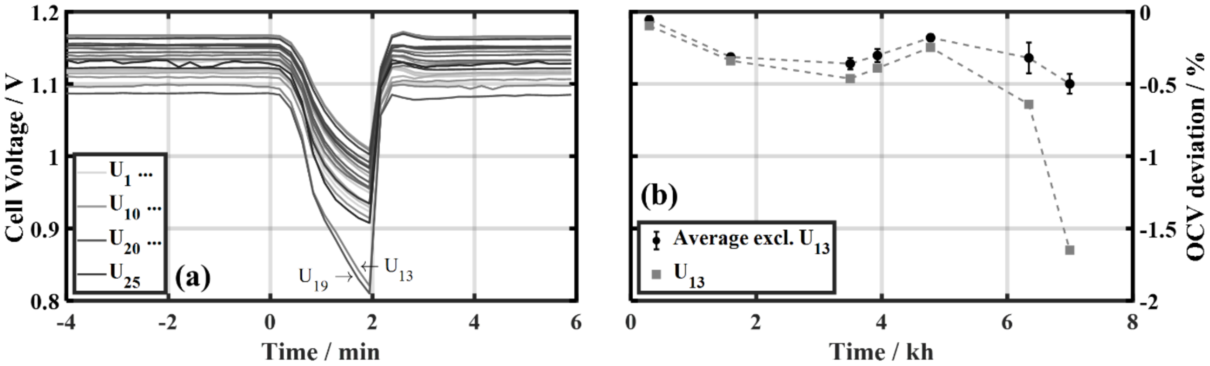

Figure 2 : (a) Initial electrochemical tightness test result (gas feed completely cut-off at 0 min from 6 NmL min^{-1} cm^{-2} of 95/5 vol% N_2/H_2), and (b) OCV deviations from Nernst calculations in 90/10 vol.% H_2O/H_2 mixtures.

3.3. Stack Disassembly

Following the test sequence and final tightness characterization at room temperature, the stack was disassembled layer by layer. The process allowed for macroscopic post-mortem observations and sample collection for SEM/EDX analyses.

No leaks were noticeable at the gas inlets and outlets of each stage of the stack. There was no clear sign of combustion inside the stack, but local interconnect oxidation was observed, particularly at the air inlets and outlets. Given the test data recorded throughout the test, particular attention was given to RU13. However, no evident signs of cermet oxidation could be detected. If Ni oxidation did occur, it was either on a fraction only of the cermet thickness so as to not be visible to outside observations, or NiO was reduced back to metallic Ni during the temperature ramp down to ambient in N_2/H_2.

Observing active areas suggested homogeneous electrical contacts. This was particularly evident on the cermet sides, where the distribution of indentations left by the Ni mesh was uniform (Figure 3a). In addition, delamination was observed on most of the O_2 electrodes. Through graphical analysis (ImageJ software), a maximum of 12% and 15% of active area delaminated was quantified on cells 12 and 13, respectively (Figure 3b). In the stack cross-flow configuration, the air inlet area was most affected. A comprehensive analysis of active area delaminated was then compared to the slopes of RU voltages over time. In spite of a small tendency, no direct and evident correlation could be determined, suggesting that delamination may not have been the main phenomenon responsible for voltage heterogeneity.

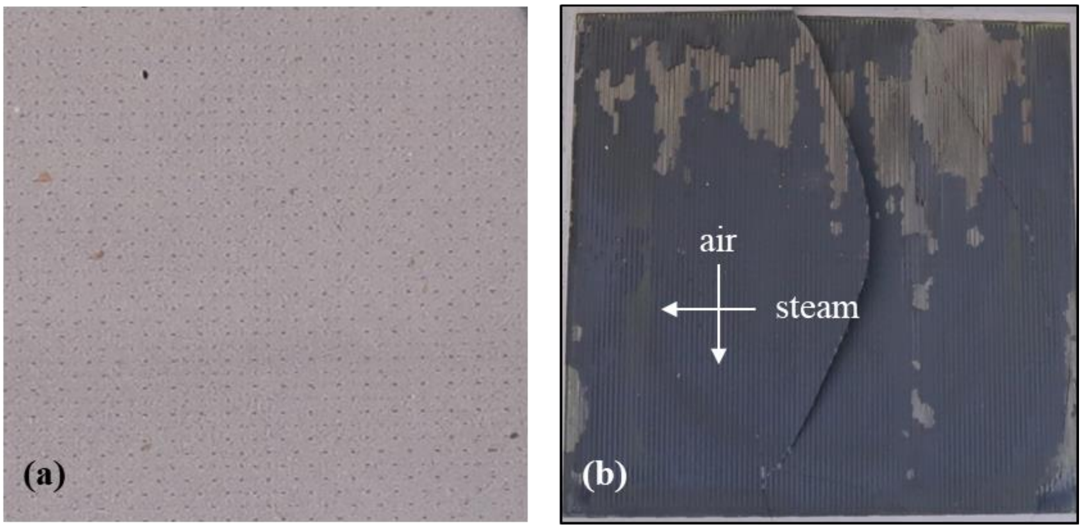

Figure 3 : (a) Picture of the imprint of the Ni contact mesh on a H_2 electrode, and (b) picture of cell 13 (10x10 cm) showing significant delamination of the O_2 electrode.

3.4. Post-Mortem Characterization of Cells

The voltages of RUs 15 and 22, shown in Figure 4, remained quite close to 1.29 V and the stack average throughout the complete test sequence. Consequently, the two cells were selected for further characterization by SEM. While similar observations were made on both, analysis of cell 22 yielded clearer micrographs, which are presented in Figure 5.

For the hydrogen electrode, the interface between the electrode and the electrolyte was specifically observed. Figure 5c highlights a migration of the Ni particles away from the interface with the electrolyte following the 6.7 kh test sequence. This result is in agreement with observations made previously in the literature for Ni-YSZ cells aged in electrolysis mode [41–43]. Additional SEM characterizations have been performed on samples extracted from the H_2O/H_2 inlet and outlet. However, in regard to the Ni migration, there is no clear differences with the center part of the cell, which is shown in Figure 5c. It is worth noting that the strong Ni depletion should induce a significant loss of performances [41,42], with additional ohmic contribution [44] and higher activation overpotential loss due to the reduction of the active reaction sites [45].

Regarding the oxygen electrode, the GDC barrier layer of the aged cell has been imaged (Figure 5d). On this picture, a dark grey phase can be observed at the interface between the YSZ electrolyte and the GDC barrier layer. EDX maps confirmed the presence of Sr and Zr in these particles, allowing them to be considered as strontium zirconates $SrZrO_3$ (SZO). Indeed, similar particles have been already observed and identified in the literature as SZO at cell [43,46,47] and stack [18,19,48] levels. The microstructure of a pristine cell following the nickel reduction procedure of the hydrogen electrode is also shown in Figure 5a and b. The micrographs show that SZO particles are already appearing after manufacturing of the cell and are observed all along the YSZ/GDC interface. The quantity appears similar to the pristine electrode, but would need to be confirmed with complementary techniques. In any case, the SZO formation might be associated to a compositional change of the O_2 electrode due to a demixing in Sr and consequently a probable loss of conductivity of this electrode from the very beginning of the cell's life. In addition to the SZO, another phase has been detected all along the surface of the GDC layer at the interface with the LSC electrode only for the aged sample (Figure 5d). EDX maps do not allow a clear identification of this phase. However, this layer seems to be mainly composed of Ce, Gd and Sr. If insulating, this secondary phase at the electrode/barrier layer interface could affect the performances. Finally, the top surface of the oxygen electrode has also been characterized as seen in Figure 5e. Some secondary phases located in the porosity were found. The elemental analyses revealed a Sr-rich composition in addition to some pollutants such as Cr and Al that could originate from the interconnects, the glass seals or the raw materials. The presence of this additional phase reveals a potential decomposition of the oxygen electrode material. Moreover, the gas diffusion and electrical contact with the current collector could be also affected by the presence of this phase.

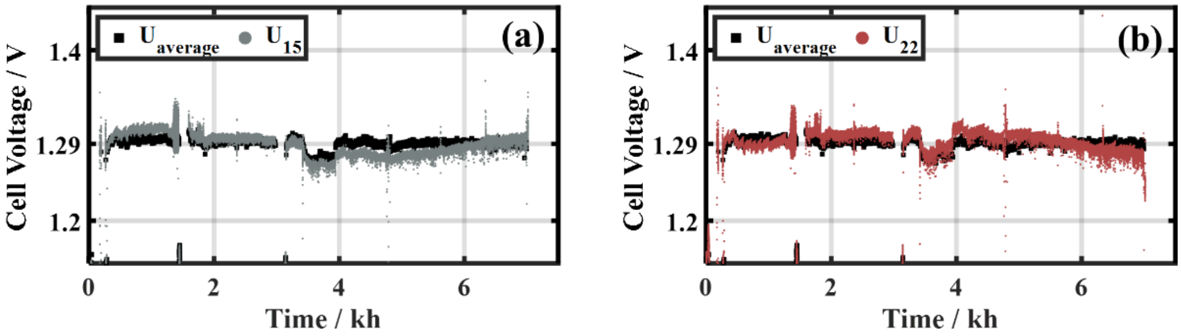

Figure 4 : Voltages of (a) repeating unit – RU – 15 and (b) RU 22 over the complete duration of the test.

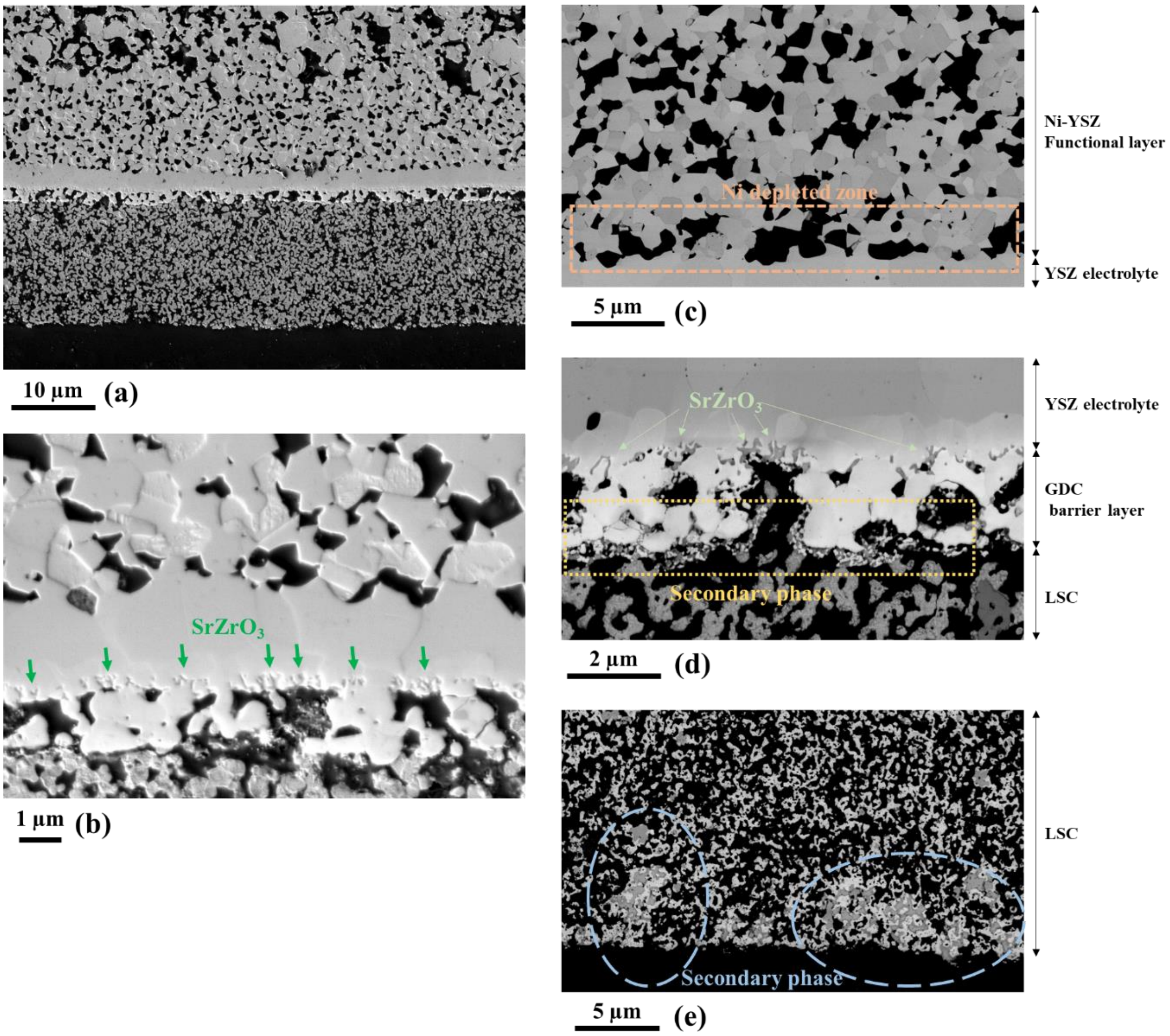

Figure 5 : SEM images of (a) and (b) a pristine cell after Ni reduction, and of the center of cell 22 (c) at the interface between electrolyte and hydrogen electrode, (d) around the barrier layer in the oxygen electrode and (e) at the top surface of the oxygen electrode.

Further analysis by ToF-SIMS allowed confirming the presence of Cr on the top of the oxygen electrodes. This chemical element was located in specific areas where Sr was also concentrated, indicating the possible formation of poorly conductive $SrCrO_4$ oxide as described in the literature [18]. This phenomenon appeared more pronounced at the gas outlets than at the inlets for both stream directions, as shown in Figure 6 using H_2O/H_2 as an example. Finally, it is worth nothing that based on the characterization techniques employed in this work, no Si could be detected in the cells.

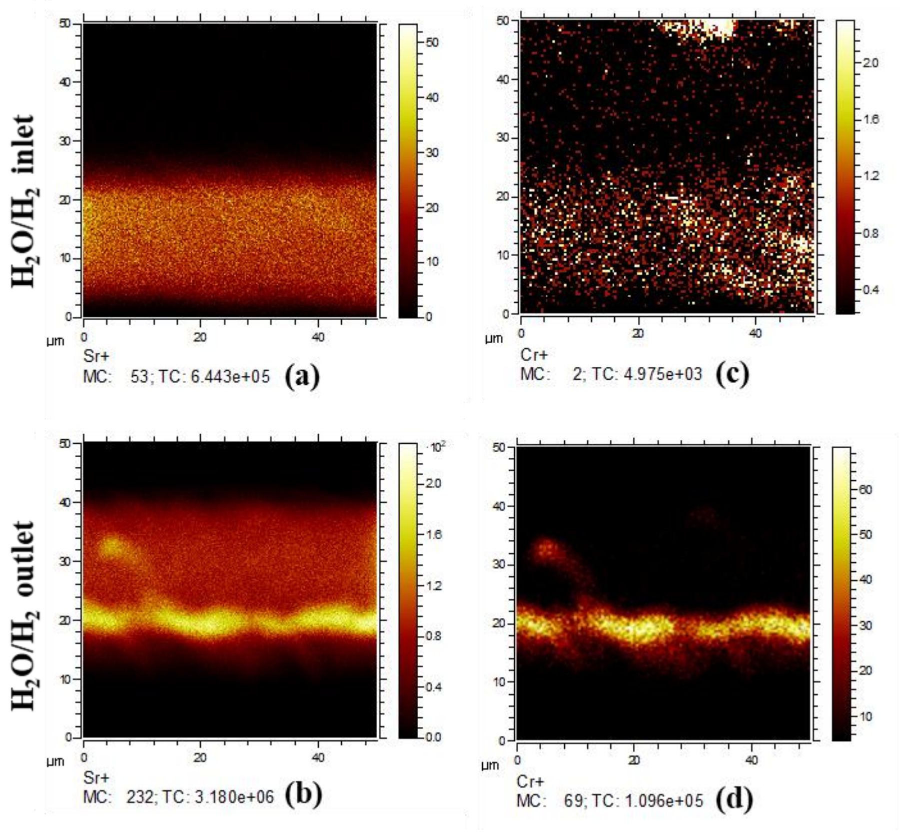

Figure 6 : ToF-SIMS maps of Sr (a & b) and Cr (c & d) recorded in the oxygen electrode at the inlet (a & c) and outlet (b & d).

Overall, in spite of RUs 15 & 22 nominal behaviour over the complete test duration, post-mortem analyses carried out in this work showed strong microstructural changes when compared to pristine cells. Nevertheless, taking into account (i) the thermoneutral operational strategy and (ii) the temperature after 6.7 kh that was still quite low (765°C) and could have technically been increased much further, it seems unlikely that the observed microstructural changes would have precipitated the stack end-of-life in the short term. However, they are expected to remain one of, if not the main contributor to the general degradation of the stack electrical response.

3.5. Post-Mortem Characterization of Interconnects

The analysis of different interconnect samples by SEM/EDX technique allowed the evaluation of phases present in the close region of the AISI441 interconnect surface on both fuel and air sides. On the air side, four distinct layers were observed (Figure 7): (i) an internal oxidation zone close to the steel surface where dispersed Ti oxide and (Fe,Nb) metallic particles (most probably Fe_2Nb Laves phase) were detected, (ii) a discontinuous Si oxide layer at the steel surface and (iii) a Cr and (Cr,Mn) oxide bilayer on top, covered by (iv) the LSM current collector. All layers looked well adherent.

Thanks to small Nb addition in the AISI441 steel matrix, (Fe,Nb) metallic particles are initially present at the grain boundaries of the interconnect material to trap Si of the steel bulk and limit poorly conductive SiO_2 formation (10^{-5} to 10^{-7} S cm^{-1} at 800 °C for crystalline and amorphous silica). They are also expected to prevent cations diffusion from steel bulk to steel surface [49]. Like Ti oxides that gathered at the steel surface, they still looked dispersed after this long-term SOEC operation. It can be noticed here that Ti oxide could improve chromia adhesion on steel while (Fe,Nb) particles could show the negative reverse effect [50].

The discontinuous thin Si oxide layer (< 1 µm) observed at the steel/Cr oxide interface is already mentioned for this steel in literature [51] and proves that unfortunately Laves phase is not able to capture all the Si amount of the steel bulk [49]. This layer could have a positive effect in limiting chromia growth [52]. Nevertheless, it could be detrimental from an electrical point of view (i.e. strong Area Specific Resistance (ASR) increase) if it becomes continuous throughout the targeted >40 kh lifetime of SOEC devices. This negative effect may be softened if doping by surrounding elements fortunately makes it more conductive. Another drawback could lie in the low thermal expansion coefficient of this phase compared to adjacent materials (4×10^{-6} K^{-1} [53] against 9.6×10^{-6} K^{-1} [54] for chromia and 12.2×10^{-6} K^{-1} [55] for AISI441 steel, up to 800°C), possibly leading to delamination of the steel/oxide layers interface during thermal cycling [55–57].

In oxidizing atmosphere at temperatures ranging from 670 to 765°C, AISI441 steel is well-known to form a layer of chromia on its surface with a (Cr,Mn) spinel phase on top [49]. Positively, those oxides are highly protective against catastrophic oxidation of the steel and fast Fe oxide formation as shown here. The thickness of the steel was still important after about 7 kh at high temperature and would be enough to preserve interconnect integrity for the targeted lifetime if the oxidation kinetics following a parabolic law does not change with time. Furthermore, no sign of dual effect, i.e. catastrophic "breakaway" oxidation on the air side when the interconnect is exposed to H_2 atmosphere on the other side was fortunately observed for this tested stack without any purely protective coating, as already found in literature for this steel in this temperature range [58,59]. This could be due to the too high initial operating temperature that preserves the stack from this detrimental phenomenon, the slight oxidation occurring during the stress-release thermal treatment applied to the interconnects before use or the presence of a

LSM contact layer on the interconnect air side [60,61]. Nevertheless, the about 50/50 Cr and (Cr,Mn) oxide global thickness ranged from 1.6 to 3.2 µm and probably contributed to the increase of the stack area specific resistance (ASR) at the interconnect/current collector interface, mainly due to the low electrical conductivity of chromia (0.001-0.05 S cm^{-1} at 800 °C [62]). The Cr depletion zone below the steel surface seen in Figure 7b remained also very thin and was most probably due to Si and Ti oxides presence without any alteration of the oxidation resistance of the steel. Finally, no Cr was detected in the LSM layer close to the interconnect interface by those techniques, even if LSM is a quite good Cr getter and if the (Cr,Mn) spinel is given to prevent Cr evaporation from the chromia layer by only 60-70% [63].

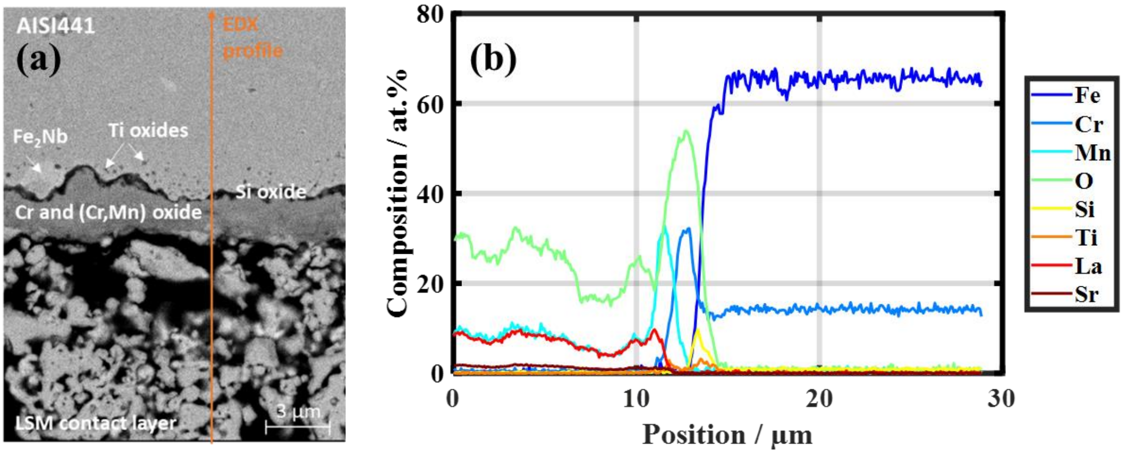

Figure 7 : (a) Cross-section of the AISI441 interconnect surface on the air side after long-term operation. (b) Elemental EDX profile measured on the orange line drawn on the picture (a).

Deeper ToF-SIMS analysis showed that Cr and Fe actually diffused from the steel in the LSM contact layer thickness as shown by the gradient of Cr and Fe content presented in Figure 8. It means that additionally to the well-known Cr vaporization from the interconnect steel [64] which probably contributed to the presence of Cr at the oxygen electrode surface (see section 3.4), Cr and Fe could also form poorly conductive phases in the LSM contact layer during long-term operating.

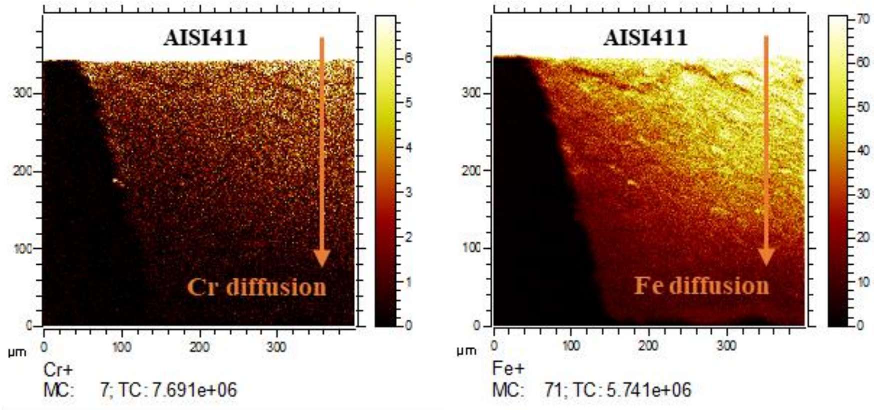

Figure 8 : ToF-SIMS maps of Cr and Fe recorded at the interconnect/contact layer interface.

On the H_2/H_2O side, a similar oxides assembly with similar thicknesses is observed on the interconnect surface after stack operation (Figure 9). It shows that oxides growth was not drastically different in presence of hydrogen and steam in this case. At the sample scale, literature results are contradictory in this respect, with either increased or decreased oxide growth kinetics, with or without iron oxide formation, mentioned in this fuel atmosphere [55,65–72]. At stack level, Linder et al. [73] observed a thicker oxide on the fuel side compared to the air one after 40 kh SOFC operation of a Galileo system from Hexis at 900 °C. Nevertheless, the electrical conductivity of chromia is depicted lower in H_2/H_2O mixture than in air, inducing a possible higher contribution of this layer to global stack degradation [66].

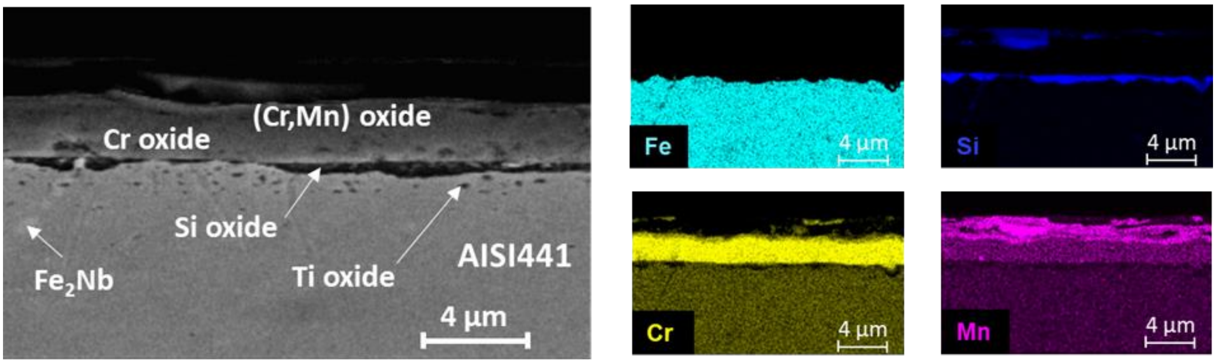

Figure 9 : Cross-section (a) and elemental EDX maps (b) of the AISI441 interconnect surface on the H_2/H_2O side after long-term operation.

Interestingly, the interface between the steel and the Ni grid ensuring electrical current distribution between the interconnect and the hydrogen electrode was also analyzed by

SEM/EDX on fuel side. In Figure 10, an interdiffusion zone is clearly visible at the contact area, where Fe, Cr and Mn moved from the steel to a Ni wire and Ni from the grid to the steel. Thanks to Cr and Mn diffusion, few (Cr,Mn) oxides were formed at the Ni grain boundaries close to the interface. Additionally, Si oxides are present at those grain boundaries in the overall section and at the periphery of the wire. Nevertheless, those poorly conductive oxides remained discontinuous at the steel/Ni interface, allowing a satisfying current path in the stack, as already shown in literature [74]. The Ni diffusion to an about 50 µm depth in the steel is prone to change the steel structure from ferrite to austenite in this area, which could reduce the Cr diffusion in the steel and may locally result in poorer high temperature oxidation resistance [75,76].

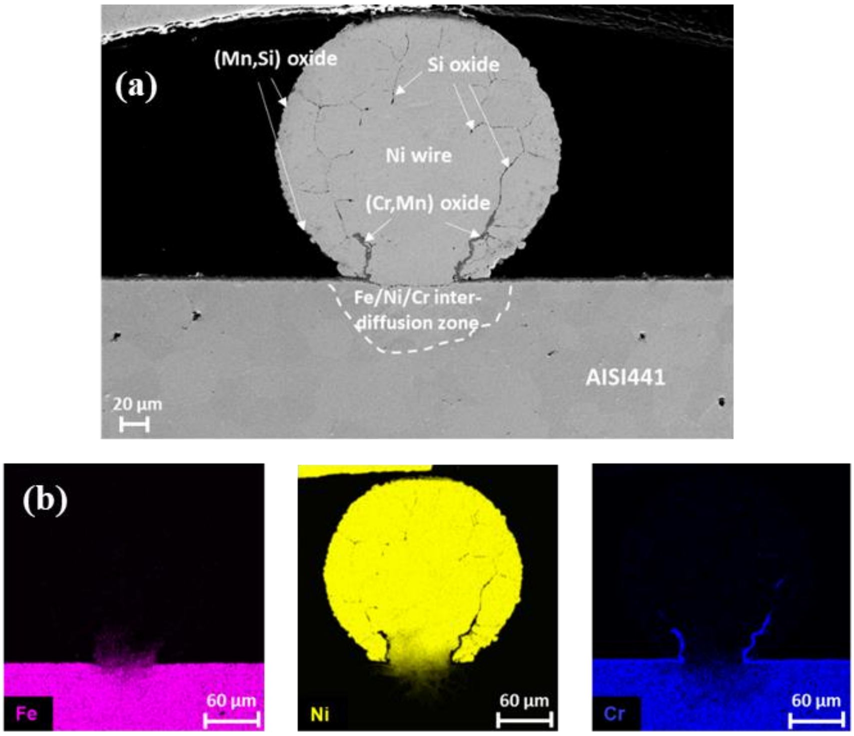

Figure 10 : Cross-section (a) and elemental EDX maps (b) of the interconnect/Ni grid interface on the H_2/H_2O side after long-term operation.

3.6. Post-Mortem Characterization of Glass Ceramic Seals

The glass-ceramic obtained by heat treatment of the glass powder (48h, 750°C) has already been described [77]. Figure 11a displays a SEM image characteristic of its microstructure. In addition to the residual glassy matrix, three different crystalline phases are observed: a Ba-rich phase (light grey polyhedral crystals, 1 to 10 µm), a Mg-rich phase (dark slats, L=150 µm, l=2 to 10 µm) and a minority Al-rich phase (very small needle-like dark crystals, L~5 µm, l < 1µm), as indicated by the cartography (Figure 12a). Additional EDX and XRD analyses allowed us to further identify the former two main phases, respectively $Ba_5Si_8O_{21}$ and $BaMg_2Si_2O_7$ [77]. The last one is a barium-aluminum silicate and despite the small quantities observed, the corresponding stoichiometry is believed to be $BaAl_2Si_2O_8$ [28].

Figure 11b and Figure 12b compare SEM images and elemental EDX cartographies of the above-mentioned heat-treated glass powder sample to the seal sample taken from the 6.7 kh-stack. The same phases are observed and identified with similar morphologies. However, the contrast between the barium silicate crystals and the residual matrix seems lower in the case of the sample from the stack. $Ba_5Si_8O_{21}$ crystal morphology appears less angular, which indicates that they may be in the process of being dissolved. In addition, barium-magnesium silicates tend to be wider compared to the 750°C-48 h heat treatment. At least, the quantity of Al-rich crystals seems higher after 6.7 kh than after 48 h. Those results are consistent with the residual matrix composition. Indeed, for the seal sample from the aged stack, the residual matrix is almost completely depleted of Mg and Al, which was not the case for the glass powder heat-treated for 48 h.

These results indicate that the seal sample contains the same crystalline phases as the glass-ceramic heat-treated at 750°C for 48h. Nevertheless, the enlargement of the magnesium barium silicate crystals and the increased crystallization of the Al-rich crystals resulted in a total depletion of Mg and Al in the residual matrix. Equilibria between residual glass and crystals are subjected to change (with time, temperature and atmosphere), but the glass-ceramic showed minimal evolution following the complete test sequence.

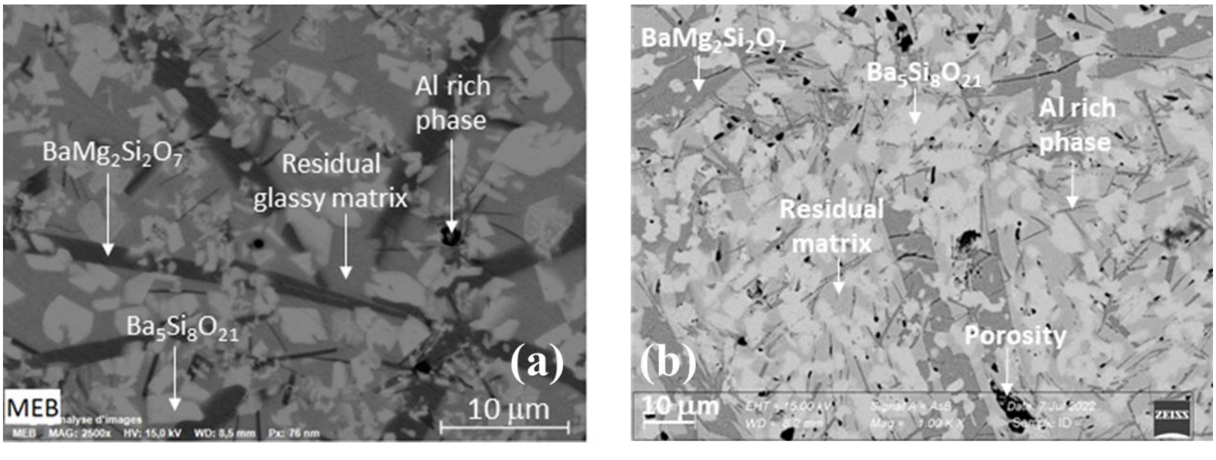

Figure 11: BSE-SEM image of (a) the glass powder sample heated at 750°C for 48 hours (from [77]) and (b) a seal sampled from the studied stack (heated for 6.7 kh between 672°C and 760°C).

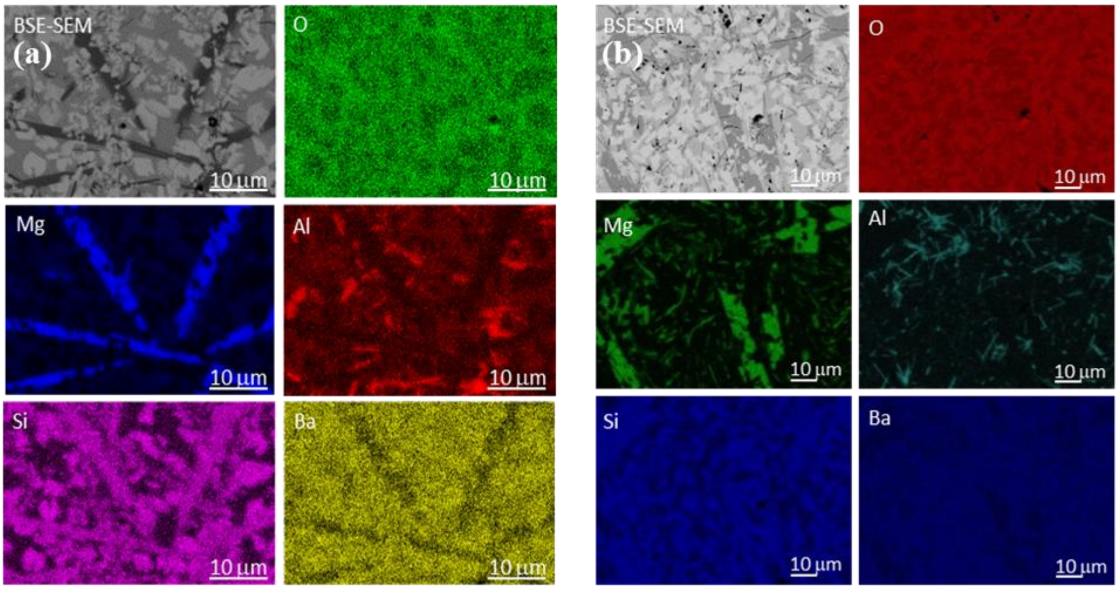

Figure 12: Elemental EDX cartography of (a) the glass powder sample heated at 750°C for 48 hours (from [77]) and (b) a seal sample of the studied stack (heated for 6.7 kh between 672°C and 760°C).

4. Conclusions

A proprietary stack comprising a self-clamping solution and 25 commercial cathode-supported cells was operated for 6.7 kh in electrolysis mode and near-thermoneutral conditions via temperature adjustments. Due to this operating strategy, the stack temperature evolved over time from an initial 672°C to about 760°C at the end of the test sequence.

Over time, individual cell voltages showed increasing levels of heterogeneity, with a voltage dispersion steadily growing from an initial 70 mV to a final 466 mV. One cell in particular (C13), that may have initially exhibited a small tightness defect further exacerbated by a failure of laboratory heating system, mainly accounts for that dispersion, with a final voltage above 1.6 V. Its OCV in 90/10 vol% H_2O/H_2 mixtures was recorded dipping beyond 5 kh, suggesting early signs of cell failure that would have likely precipitated the stack end-of-life had the test continued.

SEM imaging of the cross-sections of two cells that remained in quasi-thermoneutral conditions over the complete test sequence, C15 and C22, showed significant microstructural changes compared to pristine cells. Strong Ni depletion was evidenced at the H_2 electrodes, although no clear impact of sample position (H_2O inlet vs. center of the cell vs. H_2O outlet) could be distinguished. The formation of a SZO phase at the YSZ/GDC interface was observed, while an unidentified phase mainly containing Ce, Gd and Sr was observed at the GDC/LSC interface. Finally, secondary phases observed in pores close to the O_2 electrode surface could suggest electrode decomposition.

Concerning interconnects, the classical Cr and (Cr,Mn) oxides were observed at the AISI441 steel surface on both air and H_2O/H_2 sides. Following the test sequence, their overall thickness was comprised between 1.6 and 3.2 µm. Interestingly but not surprisingly, in these testing conditions, neither catastrophic "breakaway" oxidation nor significant Cr depletion was detected in the active areas on any side. The presence of a Si oxide layer did not appear detrimental so far, as it remained discontinuous. Additionally, it was shown that the current path between the Ni grid current collector and the interconnect was still satisfying at this stage. Nevertheless, to reduce further the stack average degradation, application of efficient protective coatings could be implemented on both interconnect sides to slow down the growth of the poorly conductive Cr and (Cr,Mn) oxides and prevent Cr penetration into the O_2 electrode and the LSM contact layer.

Finally, the microstructure of glass-ceramic seals sampled from the stack post-mortem was analyzed and compared to that of a reference sample aged for 48 h at 750°C. Results showed that both samples contained the same crystalline phases. Changes in crystal morphology and residual matrix composition did occur, but the glass-ceramic showed minimal evolution.

In the end, test data and post-mortem analyses suggest that the intrinsic stack design, comprising thin interconnects and glass-ceramic seals, is well suited for the targeted lifetimes of commercial high temperature electrolysis stacks. In the frame of the present work, loss of tightness caused by initially present cell defects and/or abnormal operational environment appears to be the main threat to pursued operation. To a lesser degree, continuous performance degradation due to cell microstructural changes and interlayer growth would lead to reaching the end-of-life temperature quicker, ultimately shortening nominal stack operation.

Acknowledgment

This work has received funding from CEA, Genvia, and the Fuel Cells and Hydrogen 2 Joint Undertaking (now Clean Hydrogen Partnership) under grant agreement No 875123. This Joint Undertaking receives support from the European Union’s Horizon 2020 research and innovation programme, Hydrogen Europe and Hydrogen Europe research.

Bibliography

[1] *The European Green Deal*, European Commission, **2019**.
[2] *A Hydrogen Strategy for a Climate-Neutral Europe*, European Commission, **2020**.
[3] *REPowerEU Plan*, European Commission, **2022**.
[4] J. Mougin, in *Compendium of Hydrogen Energy*, Elsevier, **2015**, pp. 225–253.
[5] *Strategic Research and Innovation Agenda 2021 – 2027*, Clean Hydrogen Partnership, **2022**.
[6] A. Odukoya, G. F. Naterer, M. Roeb, C. Mansilla, J. Mougin, B. Yu, J. Kupecki, I. Iordache, J. Milewski, *International Journal of Hydrogen Energy* **2016**, *41*, 7878–7891.
[7] V. Verde, E. Gurbuz, P. Olivier, A. Saker, F. Gallucci, in *16th European SOFC & SOE Forum*, Lucerne, Switzerland, **2024**, pp. 1–8.
[8] M. Lang, S. Raab, M. S. Lemcke, C. Bohn, M. Pysik, *Fuel Cells* **2020**, *20*, 690–700.
[9] C. Walter, K. Schwarze, M. Boltze, K. Herbrig, in *14th European SOFC & SOE Forum*, Lucerne, Switzerland, **2020**, pp. 29–38.
[10] A. Léon, A. Micero, B. Ludwig, A. Brisse, *Journal of Power Sources* **2021**, *510*, 230346.
[11] J. Aicart, A. Surrey, L. Champelovier, K. Henault, C. Geipel, O. Posdziech, J. Mougin, *Fuel Cells* **2023**, *23*, 463–473.
[12] J. Aicart, L. Tallobre, A. Surrey, B. Gervasoni, C. Geipel, H. Fontaine, S. Desousanobre, J. Mougin, *International Journal of Hydrogen Energy* **2024**, *60*, 531–539.
[13] J. E. O’Brien, J. L. Hartvigsen, R. D. Boardman, J. J. Hartvigsen, D. Larsen, S. Elangovan, *International Journal of Hydrogen Energy* **2020**, *45*, 15796–15804.
[14] J. Schefold, A. Brisse, H. Poepke, *International Journal of Hydrogen Energy* **2017**, *42*, 13415–13426.
[15] J. Schefold, H. Poepke, A. Brisse, *ECS Trans.* **2020**, *97*, 553–563.
[16] J. Schefold, A. Léon, C. Walter, in *15th European SOFC & SOE Forum*, Lucerne, Switzerland, **2022**, pp. 282–292.
[17] Q. Fang, C. E. Frey, N. H. Menzler, L. Blum, *Journal of The Electrochemical Society* **2018**, *165*, F38–F45.
[18] C. E. Frey, Q. Fang, D. Sebold, L. Blum, N. H. Menzler, *Journal of The Electrochemical Society* **2018**, *165*, F357–F364.
[19] G. Rinaldi, S. Diethelm, E. Oveisi, P. Burdet, J. Van herle, D. Montinaro, Q. Fu, A. Brisse, *Fuel Cells* **2017**, *17*, 541–549.
[20] M. Riegraf, P. Szabo, M. Lang, R. Costa, S. Rothe, S. Megel, M. Kusnezoff, *J. Electrochem. Soc.* **2024**, *171*, 054504.
[21] S. J. McPhail, S. Frangini, J. Laurencin, E. Effori, A. Abaza, A. K. Padinjarethil, A. Hagen, A. Léon, A. Brisse, D. Vladikova, et al., *Electrochemical Science Adv* **2022**, *2*, 1–37.
[22] G. Corre, A. Brisse, *ECS Transactions* **2015**, *68*, 3481–3490.

[23] Ro. Peters, M. Frank, W. Tiedemann, I. Hoven, R. Deja, N. Kruse, Q. Fang, L. Blum, R. Peters, *J. Electrochem. Soc.* **2021**, *168*, 014508.

[24] Ro. Peters, W. Tiedemann, I. Hoven, R. Deja, N. Kruse, Q. Fang, D. Schäfer, F. Kunz, L. Blum, R. Peters, et al., *J. Electrochem. Soc.* **2023**, *170*, 044509.

[25] A. Chatroux, M. Reytier, S. Di Iorio, C. Bernard, G. Roux, M. Petitjean, J. Mougin, *ECS Transactions* **2015**, *68*, 3519–3526.

[26] M. Reytier, C. Bernard, P. Giroud, *Stand-Alone System for Clamping a High-Temperature Soec/Sofc Stack*, **2017**, WO2017102657A1.

[27] F. Heydari, A. Maghsoudipour, Z. Hamnabard, S. Farhangdoust, *Journal of Materials Science & Technology* **2013**, *29*, 49–54.

[28] D. Gödeke, U. Dahlmann, *Journal of Power Sources* **2011**, *196*, 9046–9050.

[29] N. Lahl, K. Singh, L. Singheiser, K. Hilpert, D. Bahadur, *Journal of Materials Science* **2000**, *35*, 3089–3096.

[30] A. Chatroux, S. Di Iorio, G. Roux, C. Bernard, J. Mougin, M. Petitjean, M. Reytier, in *12th European SOFC & SOE Forum*, Lucerne, Switzerland, **2016**, pp. 222–230.

[31] J. Aicart, A. Surrey, L. Champelovier, K. Henault, C. Geipel, O. Posdziech, J. Mougin, in *15th European SOFC & SOE Forum*, Lucerne, Switzerland, **2022**, pp. 138–149.

[32] J. Mougin, A. Mansuy, A. Chatroux, G. Gousseau, M. Petitjean, M. Reytier, F. Mauvy, *Fuel Cells* **2013**, *13*, 623–630.

[33] M. Reytier, J. Cren, M. Petitjean, A. Chatroux, G. Gousseau, S. Di Iorio, A. Brevet, I. Noirot-Le Borgne, J. Mougin, *ECS Transactions* **2013**, *57*, 3151–3160.

[34] S. Di Iorio, M. Petitjean, J. Petit, A. Chatroux, G. Gousseau, J. Aicart, M. De Saint Jean, J. Laurencin, M. Reytier, J. Mougin, in *11th European SOFC & SOE Forum*, Lucerne, Switzerland, **2014**, pp. 1–8.

[35] M. Reytier, S. Di Iorio, A. Chatroux, M. Petitjean, J. Cren, M. De Saint Jean, J. Aicart, J. Mougin, *International Journal of Hydrogen Energy* **2015**, *40*, 11370–11377.

[36] J. Aicart, S. Di Iorio, M. Petitjean, P. Giroud, G. Palcoux, J. Mougin, *Fuel Cells* **2019**, *19*, 381–388.

[37] G. Cubizolles, J. Mougin, S. Di Iorio, P. Hanoux, S. Pylypko, *ECS Trans.* **2021**, *103*, 351–361.

[38] A. Hauch, A. Ploner, S. Pylypko, G. Cubizolles, J. Mougin, *Fuel Cells* **2021**, *21*, 467–476.

[39] J. Aicart, L. Tallobre, A. Surrey, D. Reynaud, J. Mougin, in *15th European SOFC & SOE Forum*, Lucerne, Switzerland, **2022**, pp. 151–162.

[40] M. Lang, Y. S. Lee, I. S. Lee, P. Szabo, J. Hong, J. Cho, R. Costa, *J. Electrochem. Soc.* **2023**, *170*, 114516.

[41] F. Monaco, M. Hubert, J. Vulliet, J. P. Ouweltjes, D. Montinaro, P. Cloetens, P. Piccardo, F. Lefebvre-Joud, J. Laurencin, *J. Electrochem. Soc.* **2019**, *166*, F1229–F1242.

[42] L. Rorato, Y. Shang, S. Yang, M. Hubert, K. Couturier, L. Zhang, J. Vulliet, M. Chen, J. Laurencin, *J. Electrochem. Soc.* **2023**, *170*, 034504.

[43] N. H. Menzler, D. Sebold, S. Zischke, *ECS Trans.* **2019**, *91*, 719–729.

[44] A. Sciazko, T. Shimura, Y. Komatsu, N. Shikazono, *JTST* **2021**, *16*, JTST0013–JTST0013.

[45] Y. Wang, C. Wu, B. Zu, M. Han, Q. Du, M. Ni, K. Jiao, *Journal of Power Sources* **2021**, *516*, 230660.

[46] J. Laurencin, M. Hubert, D. F. Sanchez, S. Pylypko, M. Morales, A. Morata, B. Morel, D. Montinaro, F. Lefebvre-Joud, E. Siebert, *Electrochimica Acta* **2017**, *241*, 459–476.

[47] F. Wang, M. Nishi, M. E. Brito, H. Kishimoto, K. Yamaji, H. Yokokawa, T. Horita, *Journal of Power Sources* **2014**, *258*, 281–289.

[48] Y. Yan, Q. Fang, L. Blum, W. Lehnert, *Electrochimica Acta* **2017**, *258*, 1254–1261.

[49] P. D. Jablonski, C. J. Cowen, J. S. Sears, *Journal of Power Sources* **2010**, *195*, 813–820.

[50] J. Mougin, M. Dupeux, L. Antoni, A. Galerie, *Materials Science and Engineering: A* **2003**, *359*, 44–51.

[51] J. W. Stevenson, Z. G. Yang, G. G. Xia, Z. Nie, J. D. Templeton, *Journal of Power Sources* **2013**, *231*, 256–263.

[52] J. Wu, X. Liu, *J. Mater. Sci. Technol.* **2010**.

[53] A. V. Mazur, M. M. Gasik, *Journal of Materials Processing Technology* **2009**, *209*, 723–727.

[54] K. Wang, Y. Liu, J. W. Fergus, *J. Am. Ceram. Soc.* **2011**, *94*, 4490–4495.

[55] M. R. Ardigo-Besnard, I. Popa, S. Chevalier, *Corrosion Science* **2019**, *148*, 251–263.

[56] S. Chandra-Ambhorn, Y. Wouters, L. Antoni, F. Toscan, A. Galerie, *Journal of Power Sources* **2007**, *171*, 688–695.

[57] N. Shaigan, D. G. Ivey, W. Chen, *Journal of Power Sources* **2008**, *185*, 331–337.

[58] M. R. Ardigo, I. Popa, L. Combemale, S. Chevalier, F. Herbst, P. Girardon, *International Journal of Hydrogen Energy* **2015**, *40*, 5305–5312.

[59] M. Bianco, P. Caliandro, S. Diethelm, S. Yang, A. Dellai, J. Van herle, R. Steinberger-Wilckens, *Journal of Power Sources* **2020**, *461*, 228163.

[60] P. Alnegren, M. Sattari, J.-E. Svensson, J. Froitzheim, *Journal of Power Sources* **2018**, *392*, 129–138.

[61] K. O. Gunduz, A. Chyrkin, C. Goebel, L. Hansen, O. Hjorth, J.-E. Svensson, J. Froitzheim, *Corrosion Science* **2021**, *179*, 109112.

[62] H. Falk-Windisch, J. Claquesin, M. Sattari, J.-E. Svensson, J. Froitzheim, *Journal of Power Sources* **2017**, *343*, 1–10.

[63] M. Stanislowski, J. Froitzheim, L. Niewolak, W. J. Quadakkers, K. Hilpert, T. Markus, L. Singheiser, *Journal of Power Sources* **2007**, *164*, 578–589.

[64] J. Froitzheim, H. Ravash, E. Larsson, L. G. Johansson, J. E. Svensson, *J. Electrochem. Soc.* **2010**, *157*, B1295.

[65] S. Fontana, S. Chevalier, G. Caboche, *Journal of Power Sources* **2009**, *193*, 136–145.

[66] S. Guillou, C. Desgranges, S. Chevalier, *Oxid Met* **2013**, *79*, 507–516.

[67] M. R. Ardigo, I. Popa, S. Chevalier, S. Weber, O. Heintz, M. Vilasi, *Oxid Met* **2013**, *79*, 495–505.

[68] L. Niewolak, D. J. Young, H. Hattendorf, L. Singheiser, W. J. Quadakkers, *Oxid Met* **2014**, *82*, 123–143.

[69] R. Sachitanand, M. Sattari, J. -E. Svensson, J. Froitzheim, *Fuel Cells* **2016**, *16*, 32–38.

[70] M. R. Ardigo-Besnard, I. Popa, O. Heintz, R. Chassagnon, M. Vilasi, F. Herbst, P. Girardon, S. Chevalier, *Applied Surface Science* **2017**, *412*, 196–206.

[71] S. Molin, Å. H. Persson, T. L. Skafte, A. L. Smitshuysen, S. H. Jensen, K. B. Andersen, H. Xu, M. Chen, P. V. Hendriksen, *Journal of Power Sources* **2019**, *440*, 226814.

[72] J. Mikkola, K. Couturier, B. Talic, S. Frangini, N. Giacometti, N. Pelissier, B. R. Sudireddy, O. Thomann, *Energies* **2022**, *15*, 1168.

[73] M. Linder, T. Hocker, L. Holzer, K. A. Friedrich, B. Iwanschitz, A. Mai, J. A. Schuler, *Journal of Power Sources* **2013**, *243*, 508–518.

[74] Y.-S. Chou, J. W. Stevenson, J.-P. Choi, *Journal of Power Sources* **2014**, *257*, 444–453.

[75] J. Malzbender, P. Batfalsky, R. Vaßen, V. Shemet, F. Tietz, *Journal of Power Sources* **2012**, *201*, 196–203.

[76] S. M. Groß-Barsnick, Q. Fang, P. Batfalsky, L. Niewolak, L. Blum, W. J. Quadakkers, *Fuel Cells* **2019**, 84–95.

[77] A. Laplace, J.-G. Begos, C. Vallat, E. Regnier, R. Moles, E. Brackx, L. Schintu, K. Vulliez, *ECS Trans.* **2023**, *111*, 2369–2376.